Research Square

Preprints are preliminary reports that have not undergone peer review.
They should not be considered conclusive, used to inform clinical practice,
or referenced by the media as validated information.

p-n Heterojunction-based Thermoelectric Generator for Highly Efficient Cancer Thermoelectric Therapy

Chao Pan
Tianjin University
Meitong Ou
Sun Yat-sen University
Ying Wang
Sun Yat-sen University
Qicai Xiao
Sun Yat-sen University
Lin Mei
Chinese Academy of Medical Sciences and Peking Union Medical College
Xiaoyuan Ji (jixiaoyuan@tju.edu.cn)
Tianjin University

Article

Keywords: Photothermal therapy (PTT), thermoelectric therapy (TET)

Posted Date: March 17th, 2021

DOI: https://doi.org/10.21203/rs.3.rs-319797/v1

License: This work is licensed under a Creative Commons Attribution 4.0 International License.
Read Full License

Abstract

Photothermal therapy (PTT) based on the light-heat conversion principle has attracted extensive attention in preclinical research, however, the hyperthermia resulted the treatment-related damage to surrounding tissues prevents further advanced clinical practice. Here, we developed a thermoelectric therapy (TET) based on p-n heterojunction ($SrTiO_3/Cu_2Se$ nanoplates) on the principle of light-heat-electricity-chemical energy conversion, demonstrating great potential for cancer treatment. The principle of TET is based on light-heat-electricity-chemical energy conversion, regarded as an upgraded version of PTT. Upon laser irradiation and subsequently natural cooling-induced the mild temperature gradient (35-45 ^oC), a self-build-in electric field was constructed and thereby facilated electrons and holes separation in bulk $SrTiO_3$ and Cu_2Se. Importantly, the contact between $SrTiO_3$ (n type) and Cu_2Se (p type) constructed another interficial electric field, which further guided the seperated electrons and holes to transfer to re-locate onto the surfaces of $SrTiO_3$ and Cu_2Se, respectively. The formation of two electric fields in bulk and interface of $SrTiO_3/Cu_2Se$ nanoplates minimized probability of charges recombination. Of note, high-performance superoxide radicals ($\cdot O_2^-$) and hydroxyl radicals ($\cdot OH$) generation from O_2 and H_2O under catalization by seperated electrons and holes, led to intracellular ROS burst and cancer cells apoptosis without apparent damage to surrounding tissues. As far as it is known, this is the first report on TET based a p-n heterojunction in biomedical field. Construction of bulk and interficial electric fields in heterojunction for improving charges separation and transfer is also expected to provide a robust and universal strategy for diverse applications including energy, environment, and biomedical engineering.

Introduction

Photothermal therapy (PTT), which is based on light-heat conversion, has aroused comprehensive attention and emerged as a potential cancer treatment strategy due to its spatiotemporal addressability, minimal invasiveness, and short treatment time.[1-4] To achieve a high anticancer efficiency, two essential criteria of traditional PTT should be considered, including high photo-thermal conversion performance of the employed photothermal agent (PTA) and long light penetration with minimized tissue scattering and absorption.[5,6] Typically, photothermal conversion efficiency is the critical factor for an eligible PTA, and it is quite necessary for a PTA to increase the temperature of the tumor site above 50 ^oC for achieving a desired therapeutic outcome. Spurred by recent progress in nanotechnology, various PTAs, including gold nanostructure,[7-10] carbon nanomaterials (graphene and its analogs),[11-17] and the recently developed two-dimensional nanomaterials (transition metal dichalcogenides (TMDCs), carbides and nitrides (MXenes), and monoelemental materials (Xenes))[18-24], have currently emerged as efficient materials for PTT-mediated cancer treatment. Additionally, in order to improve light penetration, great endeavors have been devoted to develop the second near infrared ray-based materials (NIR-II) in the spectra range of 1000-1350 nm, which possesses deeper tissue-penetration, reduced light scattering, and higher skin permissible exposure (MPE) than that of NIR-I light.[25-29] Nevertheless, only limited examples of NIR-II PTAs have been reported. Besides, the tissue-penetration of NIR-II light was greatly affected by the strong

absorbance band of water overtone, causing potential thermal damage to normal organs and tissues.[30-33] Therefore, despite these great advances achieved to date, most of the existing PTTs are not specifically related to cancer-associated events. That is, although light irradiation could target the tumor site, hyperthermia induced by conventional PTAs or ambient fluid body, would randomly propagate and diffuse to the surrounding normal tissues and organs, and thus results in the treatment-related toxicity and side effects, which are the major obstacle preventing further advanced clinical practice of PTT.

Over the last few decades, thermoelectric (TE) materials, through converting heat to electricity via electron-hole pairs separation under temperature gradient-induced the build-in thermoelectric field, have attracted tremendous attention worldwide in materials science and solid-state physics, due to their wide application in Peltier cooling and waste energy harvesting. [34-40] Further analysis of the mechanism of TE materials shows the separated electron-hole pairs under build-in thermoelectric field demonstrating great potentials in catalyzing reactive oxygen species (ROS) generation in cushy conditions, similar with the mechanisms of photodynamic therapy and piezocatalytic therapy.[41,42] In addition, compared with PTT-generated hyperthermia, the ROSs have much shorter lifetime and propagation distance *in vivo*, presumably guaranteeing much less treatment-related side effect or toxicity on surrounding normal tissues and organs. Although TE generators have grown into superstars in the application fields of energy and environment, it is still an infant in biomedical fields. Typically, the thermoelectric figure of merit is the key to evaluate the efficiency of TE materials, $ZT = S^2sT/k$, where S, s, T and k represents Seebeck coefficient, electrical conductivity, temperature, and thermal conductivity, respectively.[43,44] Obviously, the thermoelectric efficiency not only relates to physicochemical properties of TE materials, such as Seebeck coefficient, electrical conductivity, and thermal conductivity, but it also has a linear correlation with the operating temperature, in which higher temperature endows more effective electron-hole pairs separation and higher thermoelectric efficiency, which is also the main obstacle for applications in biomedical fields of TE materials.[45] Based on our previous studies,[46-50] heterojunction construction, including p-n junction and Z scheme junction, has been demonstrated as an efficient strategy for improving electron-hole pairs separation and enhancing the catalytic efficiency. After contacting of p-type and n-type semiconductors, the interfacial electric field will be constructed, in which the separated electrons and holes in both semiconductors would transfer in the opposite direction and locate in different semiconductors.[51-54] The unfavorable recombination of electron-hole pairs would be retarded, which is the key for conversion efficiency of photocatalysts, electrocatalysts, and TE materials.

Herein, for the first time, we developed a novel thermoelectric therapy (TET) based on light-heat-electricity-chemical energy conversion, by employing $SrTiO_3$ (n type) and Cu_2Se (p type) to construct a p-n heterojunction, which is capable of dual independently targeted generating ROS under mild temperature gradient (from 35 ^oC to 45 ^oC). As shown in Figure 1, by employing conventional two-step hydrothermal processes, $SrTiO_3/Cu_2Se$ based p-n heterojunction was constructed. Under 808 nm laser irradiation and natural cooling, the electrons and holes in the bulk of $SrTiO_3$ and Cu_2Se voluntarily separate and migrate from the bulk to the surface under the driving force of the build-in thermoelectric field on the opposite

directions. Additionally, the p-n heterojunction between $SrTiO_3$ and Cu_2Se constructs an interfacial electric field, and thus redistributes the surface electrons and holes to specific locations for reduction and oxidation reactions, respectively, which further restrains the undesired recombination of electrons-hole pairs in the bulk and on the surface of TE materials. Consequently, a ROS burst under mild temperature gradient and low concentration of TE materials was provided based on a thermoelectric effect. With the goal of complete remission of tumors and without recurrence, our work here presents a novel thermoelectric mechanism based on p-n heterojunction constructed TE generator, with dual independently targeted ROS bursts for efficient cancer therapy and with negligible side effects towards normal tissues. To be noted, we also anticipate the performances of such a p-n heterojunction-constructed TE generator in other settings of biomedical applications beyond cancer treatment.

Results And Discussion

Preparation and characterization of $SrTiO_3/Cu_2Se$ p-n heterojunction

In the first stage of this work, the $SrTiO_3/Cu_2Se$ p-n heterojunction was synthesized through two steps of hydrothermal process. Detailly, as illustrated in Figure 1, $SrTiO_3$ nanoplates (NPs) (n type TE materials) were papered firstly following Cu_2Se quantum dots (QDs) synthesis and in site coating on the surface of $SrTiO_3$ NPs. After the hydrothermal process and liquid exfoliation, $SrTiO_3$ NPs with a size of 110 nm were analyzed by transmission electron microscopy (TEM) (Figure 2a and Figure S1). Then, Cu_2Se QDs, p type TE materials, were synthesized and coated on the surface of $SrTiO_3$ NPs, forming a novel p-n heterojunction-based TE generator. The successfully coated Cu_2Se QDs was obviously observed in the TEM images of $SrTiO_3/Cu_2Se$ NPs (Figure 2b), in which uniform QDs decoration on the surface of $SrTiO_3$ NPs was exhibited. The size of the prepared $SrTiO_3/Cu_2Se$ NPs was appropriately increased to about 132 nm (Figure S2). Additionally, the high-resolution transmission electron microscopy (HRTEM) images with clear interference fringe and *d*-spacing of 0.27 nm and 0.33 nm, corresponding to the plane of $SrTiO_3$ NPs (Figure 2c) and Cu_2Se QDs (Figure 2d), provided a direct evidence for the successful fabrication of the heterojunction structure. Besides, atomic force microscope (AFM) was also applied to characterize the morphology of the fabricated $SrTiO_3/Cu_2Se$ NPs. As shown in Figure 2d and 2e, a rough surface was clearly observed, which was likely attributed to the coating of Cu_2Se QDs. Calculation from the 2D and 3D AFM images of $SrTiO_3/Cu_2Se$ NPs, the NPs displayed a planar size of about 132 nm and thickness of 50 nm. Given that almost all thermoelectric materials have a good piezoelectric property,[55-57] we determined the piezoelectric properties of $SrTiO_3/Cu_2Se$ NPs by a piezoresponse force microscope (PFM), using dual alternating current resonance tracking (DART) modes with the aim to expel the displacement contribution from electrostatic interaction and topographical crosstalk in mapping the local electromechanical properties. Figure 2e-2h exhibited the topographic, vertical piezoresponse amplitude, and phase images of the $SrTiO_3/Cu_2Se$ NPs, respectively. The $SrTiO_3/Cu_2Se$ NPs can be clearly detected in the topographic image with clear contrast in the amplitude and phase images. Figure 2g exhibited the phase map of $SrTiO_3/Cu_2Se$ NPs, which well matches the morphology map in Figure 2e. Next, a surface potential of 30

mV of $SrTiO_3/Cu_2Se$ NPs was observed in the piezoelectric potential map of $SrTiO_3/Cu_2Se$ NPs (Figure 2h) obtained by PFM in the darkness, which demonstrates its piezoelectric property and further testifies its thermoelectric property. To further confirm the successful fabrication and the composition of $SrTiO_3$ NPs, Cu_2Se QDs and $SrTiO_3/Cu_2Se$ NPs, X-ray photoelectron spectroscopy (XPS) and X-ray diffractometry (XRD) were performed. In the XPS analysis (Figure 3a), the specific peaks of Sr, Ti, O, and Cu, Se, were exhibited in their XPS spectra, respectively. Moreover, all these characteristic peaks were observed in the XPS spectrum of $SrTiO_3/Cu_2Se$ NPs. In the XRD spectrum (Figure 3b), two respective structures corresponding with $SrTiO_3$ and Cu_2Se were observed. All above observations confirmed the successful fabrication of the heterojunction structure and their potential thermoelectric property of $SrTiO_3/Cu_2Se$ NPs.

The biomedical applications of nanomedicine largely depend on their physiological dispersibility and stability. It was observed that the surfaces of $SrTiO_3/Cu_2Se$ NPs were slightly negatively charged after the hydrothermal process, (Figure S3), which allowed surface modification by using amphipathic DSPE-PEG through hydrophobic interaction. The zeta potential of $SrTiO_3/Cu_2Se$ NPs increased to -30 mV, demonstrating a successful PEG modification and thus ensuring their physiological dispensability and stability. Around 25% (w/w) of DSPE-PEG was loaded on the surface of the $SrTiO_3/Cu_2Se$ NPs as measured by inductively coupled plasma-atomic emission spectrometry (ICP-AES). PEGylation of $SrTiO_3/Cu_2Se$ NPs showed improved dispersion in cell culture medium, phosphate buffer saline (PBS) and water in contrast with the bare $SrTiO_3/Cu_2Se$ NPs due to lack of aggregation (Figure S4). In addition, the Fourier transform infrared (FT-IR) absorption bands of the PEGylated $SrTiO_3/Cu_2Se$ NPs at ~1250 cm^{-1} and ~2900 cm^{-1} are corresponded to the C=O stretching vibration and -CH vibrations in the DSPE-PEG segment (Figures S5). Finally, Sr (red), Ti (green), and O (blue) appeared in the energy dispersive spectrometry (EDS) mapping of $SrTiO_3$ NPs, and after Cu_2Se QDs and PEG coating, Cu (purple), Se (olive), C (yellow), and N (white) showed again in the EDS mapping of PEGylated $SrTiO_3/Cu_2Se$ NPs (Figure 2i), further confirmed successful surface coating by DSPE-PEG.

Next, the thermoelectric performance of our prepared $SrTiO_3/Cu_2Se$ NPs were examined. The ZT of $SrTiO_3$ NPs and Cu_2Se QDs were tested and calculated, respectively. Figure 3c shows the material-dependent s as a function of temperature. It is apparently that s increases monotonically with increasing the temperature for these two samples and roughly follows a co-efficient of $T^{-1.5}$, suggesting that acoustic phonons dominate the carrier scattering. Figure 3d shows the variations of S with the temperature. The positive signal of S indicates the p-type nature for Cu_2Se QDs, and the negative signal of S indicates the n-type nature for $SrTiO_3$ NPs. S increases gently upon increasing the temperature. Figure 3e presents the plots of S^2s as a function of temperature, from which relatively high S^2s of $SrTiO_3$ NPs and Cu_2Se QDs were obtained. Figure 3f is the plots of κ as a function of temperature, in which the relatively low κ of $SrTiO_3$ NPs and Cu_2Se QDs were also obtained. Due to the obtained high S^2s as well as low κ, significantly enhanced ZT values are expected. Figure 3f is the ZT plots as a function of

temperature, in which a peak ZT of 0.11 and 0.17 at 333 K is achieved in the fabricated $SrTiO_3$ NPs and Cu_2Se QDs. Figure 3h shows the S at room temperature as a function of the natural logarithm of s of $SrTiO_3$ NPs and Cu_2Se QDs. This linear relationship between the S and the natural logarithm s indicates more fluctuating carrier concentration and less varying carrier mobility. All above observations confirmed the good thermoelectric properties of $SrTiO_3/Cu_2Se$ NPs.

$SrTiO_3/Cu_2Se$ NPs mediated reactive oxygen species (ROS) generation

Followingly, the light-heat-electricity-chemical energy conversion of $SrTiO_3$ NPs, Cu_2Se QDs, and $SrTiO_3/Cu_2Se$ NPs were measured and analyzed. Figure 4a and 4b show the light-heat conversion of $SrTiO_3/Cu_2Se$ NPs, in which the temperature increased from 35 ^oC to 45 ^oC under 2.5 min 808 nm laser irradiation and cooled down to 35 ^oC following 9 min natural cooling process. As shown in Figure 4h, according to thermoelectric effect, under temperature gradient (35 ^oC - 45 ^oC) induced by 808 nm laser irradiation and natural cooling, a build-in electric field was constructed on the opposite surfaces of $SrTiO_3$ NPs or Cu_2Se QDs. Therefore, the built-in electric field can facilitate separation of charges (electrons and holes) in bulk, and promote their transfer to the catalyst surface, making them effective tools for catalyzing reduction and oxidization of O_2 and H_2O to generate superoxide anion ($\cdot O_2^-$) and hydroxyl radical (·OH), respectively. $\cdot O_2^-$ generation through the reduction of electrons was measured with dihydrorhodamine 123 (DHR 123) probe. As shown in Figures 4c and 4e, obvious fluorescence increase was detected following the temperature gradient (35 ^oC - 45 ^oC) using $SrTiO_3$ NPs and Cu_2Se QDs separately, which indicated that $SrTiO_3$ NPs and Cu_2Se QDs are suitable nanomedicines for thermoelectric therapy. Of note, a much stronger fluorescence increase was observed when $SrTiO_3/Cu_2Se$ NPs were applied as thermoelectric catalysts for catalyzing $\cdot O_2^-$ generation from O_2. As exhibited in Figure 4h, after $SrTiO_3$ NPs (n type) contacting with Cu_2Se QDs (p type), an interfacial electric field was then constructed on their interface, in which the separated electrons and holes induced by thermoelectric effect further transferred and re-located on the surface of different catalysts following interfacial electric field. Thereby, the recombination of electrons and holes was restricted, leading to extending lifetime of separated electrons and holes for further redox reactions. The p-n heterojunction enhanced thermoelectric effect of $SrTiO_3/Cu_2Se$ NPs was further assessed in terms of hydroxyl radical (·OH) production using methylene blue (MB) as the specific probe of ·OH. Consistent with the above results, the $SrTiO_3/Cu_2Se$ NPs exhibited the strongest ·OH generation, which further confirmed their p-n heterojunction enhanced thermoelectric effects (Figure 4d and 4f). By employing 5,5-dimethyl-1-pyrroline N-oxide as the spin trapping agent, electron spin resonance (ESR) was applyed to detect the gnerated ROS directly. As shown in Figure 4g, $\cdot O_2^-$ and ·OH synchronously generated from $SrTiO_3/Cu_2Se$ NPs through thermoelectric effects from O_2 and H_2O were detected, which further confirms the high ability of ROS generation of $SrTiO_3/Cu_2Se$ NPs.

In vitro antitumor evaluation mediated by $SrTiO_3/Cu_2Se$ NPs

The biocompatibility of the prepared TE agents was next tested using MCF 7 and Hela cancerous cells. As shown in Figure 5a and S7, similar with the traditional photothermal agent (graphene, G), the TE agents showed negligible cytotoxicity in the absence of excitation, and more than 80% of the cells were viable even when exposed to 100 mg/mL of the respective TE agents. Stimulation with 808 nm laser led to the temperature increasing from 35 ^{o}C to 45 ^{o}C, and thus increased the cytotoxic effects of all TE agents (Figure 5b and S8). However, under the uniform 808 nm laser irradiation and temperature increase, the cells treated with G still remain a relatively high viability.To this end, we speculated that the cytotoxic effects of TE agents are probably attributed to the thermoelectric effect inducing ROS generation, rather than photothermal effect inducing heat. With increasing cycles of this temperature gradient (35 ^{o}C - 45 ^{o}C), an enhanced cell cytotoxic effects of TE agents were observed, meanwhile, the cytotoxic effects of G remain negligiblely improved. This observation further demonstrated the thermoelectric effect of TE agents inducing ROS generation was the main cause for their cytotoxicity. Moreover, the cells treated with $SrTiO_3/Cu_2Se$ NPs exhibited the highest cytotoxicity, confirming the p-n heterojunction enhanced thermoelectric effect. Additionaly, the intracellular ROS levels under different treatments were analyzed by using fluorescent probe. Indeedly, the intracellular ROS levels were signficantly higher in the $SrTiO_3$ NPs and Cu_2Se QDs treated groups, compared to those treated with G, and the highest ROS concentration was detected in cells exposed to the $SrTiO_3/Cu_2Se$ NPs coupled with 808 nm laser irradiation and a natural cooling process (Figures 5d and 5e). As previously reported,[58] DNA damage caused by ROS is one of the main causes for ROS-induced cell toxicity. Thus, the levels of DNA damage in MCF 7 cells after different treatments were further analyzed using γ-H2AX as a marker for DNA double-strand breaks. As shown in Figure 5f, MCF 7 cells treated with G with DT (35 ^{o}C - 45 ^{o}C) did not show any obvious DNA damage compared with the control group. However, MCF 7 cells treated with $SrTiO_3$ NPs or Cu_2Se QDs coupling with the same DT, showed apparently detectable levels of DNA damage, further supporting the TE effect of $SrTiO_3$ NPs and Cu_2Se QDs. Treatment with $SrTiO_3/Cu_2Se$ NPs and DT produced considerably high levels of irreparable DNA damage in the cancer cells. All these results thus suggest that the developed therapeutic strategy based on $SrTiO_3/Cu_2Se$ NPs and DT with an enhanced TE effect can specifically kill cancer cells. Moreover, the efficient apoptosis of $SrTiO_3/Cu_2Se$ NPs via TE effect was further detected through co-staining cells with propidium iodide (PI, dead cells, red fluorescence) and calcein AM (live cells, green fluorescence) after different treatments. The LSCM images of co-stained cancer cells, as shown in Figure 5g, also confirmed the antitumor effect of TET *in vitro*.

In vivo antitumor evaluation mediated by $SrTiO_3/Cu_2Se$ NPs

The anti-cancer potential of TET was next evaluated *in vivo* using MCF 7 tumor-bearing mice. The mice were each injected intravenously with Cy7-labeled NPs at the dosage of 5 mg/kg, and the fluorescence intensity of Cy7 in the blood was measured at different time intervals. As shown in Figure 6b, the Cy7-loaded NPs remained signficantly longer in circulation compared to free Cy7, which was suggestive of greater tumor accumulation of NPs. Additionally, the tumor accumulation of NPs was also confirmed by fluorescence imaging of major organs after 24 h *i.v.* injection (Figure 6c). To more precisely characterize

the biodistribution of NPs *in vivo*, an ICP was employed to test the concentration of NPs in the major organs and tumors over 24 hours, which also showed a great tumor accumulation of the prepared NPs. The MCF 7 tumor-bearing mice were randomly divided into the following groups and treated accordingly: 1) saline control, 2) $SrTiO_3/Cu_2Se$ NPs, 3) $SrTiO_3$ NPs + DT, 4) Cu_2Se QDs + DT, 5) $SrTiO_3/Cu_2Se$ NPs + DT, 6) G + DT, and 7) PTT (G, >55^oC). The DT means temperature gradient (35 ^oC - 45 ^oC) for 3 cycles inducing by 808 nm laser irradiation and natural cooling after 24 h post injection (Figure 6a and 6e). The tumor volume was measured every 2 days, and as shown in the growth curves in Figure 6f and 6g, the untreated and non-DT controls did not show any significant inhibition of tumor growth. The combination of TE agents ($SrTiO_3$ NPs or Cu_2Se QDs) and DT achieved an obvious inhibitory effect, which is attributed to the generation of ROS by the thermoelectric effect. Due to the p-n heterojunction enhanced thermoelectric effect, $SrTiO_3/Cu_2Se$ NPs with DT markedly inhibited tumor growth, in which $SrTiO_3/Cu_2Se$ NPs almost completely ablated the tumors under the same conditions. In contrast, the G NSs with the same DT treatment exhibited only a slight inhibition of tumor growth compared with the control group, which indicated the temeperature of 45^oC can not able to induce cancer cells death. Only the hyperthermia (>55 ^oC) induced by G NSs-mediated PTT could provide a similar anti-tumor effect as that of TET (45 ^oC) (Figure 6h). However, as shown in Figure 6g, because the hyperthermia (>55 ^oC) randomly propagated and diffused to the surrounding tissues, an obvious PTT-related toxicity and side effects on normal tissues was observed, in which the skin and muscle at the 808 nm laser irradiation site were scorched. By contrast, there was negligible damage to the skin at the irradiated sites of TET (45 ^oC) (Figure 6f). These findings are consistent with the thermoelectric effect and heterojunction structure of $SrTiO_3/Cu_2Se$ NPs that induces an intracellular ROS burst. The representative images of mice from the different treatments are shown in Figure 6f and 6g. Moreover, the mice treated with $SrTiO_3/Cu_2Se$ NPs + DT showed the longest lifetime without any tumor recurrence (Figure 6l). No signficant changes were observed in the body weight of the mice during the experimental period (Figure S10), indicating negligible adverse effects of this therapy *in vivo*.

The intracellular ROS burst effect was further validated by using DCFH fluorescence probe. As shown in Figure 6i and S11, the different treatments led to consistent ROS accumulation in the tumors, and the strongest green fluorescence was detected in the $SrTiO_3/Cu_2Se$ NPs + DT group, further indicating a drastic ROS burst in tumor cells. Given that ROS induce apoptosis through DNA damage,[58] we next analyzed the tumors for signs of DNA double strand breaks, oxidative stress and apoptosis. $SrTiO_3/Cu_2Se$ NPs alone induced negligible γ-H2AX foci and very few apoptotic cells, whereas both DNA damage and apoptosis were considerably higher under $SrTiO_3$ NPs or Cu_2Se QDs with DT. Coupling $SrTiO_3/Cu_2Se$ NPs and DT led to a marked increase in γ-H2AX foci and apoptosis in the tumors (Figure 6j and 6k). Furthermore, the levels of 8-hydroxy-2'-deoxyguanosine (8-OHdG), a marker of oxidized DNA, were consistent with that of γ-H2AX (Figure S12). Taken together, the p-n TE agents heterojunction can efficiently trigger a ROS burst in cancer cells and induce apoptosis under a mild condition.

Biocompatibility evaluation of $SrTiO_3/Cu_2Se$ NPs

The biocompatibility of TET was evaluated *via* hematological, histological and immunological indices. As shown in Figure 7a-7c, no obvious difference in ROS levels, DNA damage, apoptosis, and tissue damage were observed in normal tissues after treatment with $SrTiO_3/Cu_2Se$ NPs + DT compared with those treated with PBS, indicating a favorable biocompatibility of the $SrTiO_3/Cu_2Se$ NPs and TET in normal tissues. Moreover, the serum levels of IFN-γ, IL-6, TNF-α and IL-12+P40 were similar in the control and treated mice 12 and 24h post *i.v.* injection of $SrTiO_3/Cu_2Se$ NPs (10 mg/kg) (Figure 7d). In addition, routine blood examination on days 1, 7 and 14 post-injection did not show any significant differences in aspartate aminotransferase (AST), alanine aminotransferase (ALT), white blood cells (WBC), blood urea nitrogen (BUN), alkaline phosphatase (ALP), red blood cells (RBC), platelet (PLT), Hemoglobin (HGB), mean corpuscular volume (MCV), creatinine (Cr), lymphocyte (LYM), hematocrit (HCT), and neutrophil (NEU) between the control and treated groups (Figure 7e). Taken together, $SrTiO_3/Cu_2Se$ NPs and TET are biocompatible *in vivo*.

Comparation of side effects between PTT and TET

As demonstrated above, PTT with hyperthermia (>55 ^oC) could easily damage the skin at irradiated site. To further confirm the superiority of TET, we finally compared the treatment-related toxicity and side effects on normal tissues and organs through simulating the PTT and TET at some major organs and tissues. As exhibited in Figure 8, exposure to the TET (45 ^oC) conditions, negligible toxicity or side effect are observed in their H&E staining images of heart, liver, spleen, lung, kidney, muscle, and skin, compared with these without any treatment. However, obvious and serious damages were revealed in these important organs and tissues after exposing to the PTT (55 ^oC) conditions. For example, congestion, enlargement of intercellular space, tissue defect, etc, were presented in these major organs. Additionally, evident swelling and critical damage were also observed in muscle and skin under treated with PTT (55 ^oC). All above phenomena further confirmed the *in vivo* safety of TET and demonstrated competitive advantages over PTT.

Conclusions

In summary, a novel TET based on p-n heterojunction TE generator was successfully developed and demonstrated outstanding anticancer potency with negligible side-effects. The $SrTiO_3/Cu_2Se$ NPs based p-n heterojunction was prepared by simple two-step hydrothermal processes, exhibiting an excellent thermoelectric effect under mild temperature gradient from 35 ^oC to 45 ^oC. The formation of build-in electric field induced by thermoelectric effect under temperature gradient allowed directional separation of electrons and holes in the bulk of $SrTiO_3$ NPs and Cu_2Se QDs. Furthermore, the interfacial electric field induced by contacting of $SrTiO_3$ NPs (n type) and Cu_2Se QDs (p type) further guided the distribution and re-location of the excited electrons and holes onto the surface of $SrTiO_3$ NPs and Cu_2Se QDs, respectively. The synergy between build-in and interfacial electric fields facilitated the electrons and holes separation and transfer both in the bulk and the interface, minimizing the undesired charge recombination. Under 808 nm laser irradiation and natural cooling induced temeprature gradient (35-45 ^oC), the engineered

$SrTiO_3/Cu_2Se$ NPs serve as an intelligent TE generator with dually independent ROS ($\cdot O_2^-$ and $\cdot OH$) generation through catalyzing the oxidation and reduction of O_2 and H_2O in tumor microenvironment. With an effective ROS burst mediated apoptosis of cancer cells both *in vitro* and *in vivo*, the p-n heterojunction TE generator based TET has been demonstrated to be a novel and potential clinic cancer treatment. This work is also expected to provide a smart strategy for the design of other p-n heterojunction TE generator with efficient charges separation and will inspire future studies in expanding their in-depth application, especially in other biomedical applications, such as diabetic ulcer treatment and wound infection resistance under temperature difference between the body and outside environment.

Materials And Methods

Materials

$Ti(OBu)_4$, $Sr(NO_3)_2$, NaOH, $(CH_2OH)_2$, Se, CuI, $H_2N(CH_2)NH_2$, 9,10-anthracenedipropanoic acid (ABDA), $[Ru(dpp)_3]Cl_2$ (RDPP), H_2O_2 (30%), N-methyl-pyrrolidone (NMP), methylene blue (MB), 5,5'-dithiobis (2-nitrobenzoic acid) (DTNB), and dihydrorhodamine 123 (DHR123) were supplied by Sigma-Aldrich.DSPE-PEG-Cy7 (MW: 5k) and DSPE-PEG (MW: 5k) were purchased from Nanocs Inc. PBS (pH 7.4 and 5.5), DMEM medium, RPMI medium, trypsin-EDTA, and fetal bovine serum (FBS) were purchased from Gibco Life Technologies.

Synthesis of $SrTiO_3/Cu_2Se$ NPs

The $SrTiO_3/Cu_2Se$ NPs based p-n heterojunction was prepared by simple two-step hydrothermal processes. First, $SrTiO_3$ NPs were synthesized by a hydrothermal method using Teflon lined stainless steel autoclave containing the mixture of $(CH_2OH)_2$, NaOH, $Sr(NO_3)_2$, and $Ti(OBu)_4$. After the steel autoclave was heated at 180 ^oC for 24 h, the obtained powder was under probe sonication–assisted liquid exfoliation in NMP for 5 h. Then, the solution was centrifuged at 3000 rpm for 5 min to obtain $SrTiO_3$ NPs. For Cu_2Se QDs coating, CuI and Se powders were placed in a Teflon lined stainless steel autoclave containing 30 mL ethylenediamine and prepared $SrTiO_3$ NPs. After the steel autoclave was heated at 90 °C for 4 h, the precipitate was centrifuged at 3000 rpm and washed with distilled water for 3 times. Then, the prepared products were dried in vacuum at 50 °C for 4 h. The final black products ($SrTiO_3/Cu_2Se$ NPs) were collected.

For surface modification, DSPE-PEG was dissolved into the $SrTiO_3/Cu_2Se$ NPs solution and stirred for 12 hours after 30 min of sonication. Then the solution was centrifuged for 30 min at 5000 rpm with Amicon pipes (MWCO 100kDa; Millipore) and the precipitates were washed 3 times to remove the residual DSPE-PEG. The same process was used for fluorescent modification of $SrTiO_3/Cu_2Se$ NPs using DSPE-PEG-Cy7 in a dark environment.

Characterization

The zeta potential and corresponding size of $SrTiO_3/Cu_2Se$ NPs were detected through Dynamic Light Scattering. The morphology of $SrTiO_3/Cu_2Se$ NPs was observed with transmission electron microscopy (TEM, JEM-2100UHR, JEOL, Japan) and atomic force microscopy (AFM, FASTSCANBIO, Germany). Piezoresponse force microscopic (PFM) measurements were characterized by an AFM (NTEGRA, NT-MDT, Russian) equipped with a ferroelectric test system. The $SrTiO_3/Cu_2Se$ NPs chemical constituents were detected by energy-dispersive X-ray spectroscope (EDS) (Inca X-MAX, Oxford, UK), X-ray photoelectron spectroscopy (XPS, ESCALAB 250Xi, Japan), and fourier transform infrared spectrophotometry (FTIR, Nexus 470, Nicolet, Madison, WI, USA). The $SrTiO_3/Cu_2Se$ NPs chemical structures were characterized by employing X-ray powder diffraction (XRD, Bruker D8 multipurpose). As for thermoelectric properties, a laser flash method (LFA 457, NETZSCH) was utilized to measure thermal diffusivity (D), while a ZEM-3, ULVAC was used for the analysis of s and S.

- **OH production in vitro**

The mixture of $SrTiO_3$ NPs, Cu_2Se QDs or $SrTiO_3/Cu_2Se$ NPs and MB were prepared in PBS (pH 7.4) and stirred for 1 hour in a dark environment at the corresponding final concentration of 0.050 mg/mL TE agents and 0.05 mg/mL MB, respectively. Then the mixture was irradiated with 808 nm laser (1 W/cm^2) for 2.5 min and cooled naturally for 10 min. The diminished MB was determined by recording the absorption of the supernatant via UV-vis spectroscopy.

- **O_2^- production in vitro**

The mixture of $SrTiO_3$ NPs, Cu_2Se QDs or $SrTiO_3/Cu_2Se$ NPs (0.05 mg/mL) and DHR123 (1 μL,1 mM) were formed in PBS (pH 7.4) and stirred for 1 hour in a dark environment. Then the mixed solution was irradiated via 808 nm laser (1 W/cm^2) for 2.5 min and natural cooling for 10 min. The changing fluorescence of DHR123 was recorded by fluorescence spectrophotometer.

Electron Paramagnetic Resonance (EPR) for ·OH and $\cdot O_2^-$ in vitro

For further detection of the ·OH and $\cdot O_2^-$ formation, $SrTiO_3/Cu_2Se$ NPs (0.05 mg/mL) and 5,5-dimethyl-1-pyrroline N-oxide (DMPO) (0.1 mM) were fully mixed (solution for testing ·OH: DI water, solution for testing $\cdot O_2^-$: methanol). The respective signals were analyzed by Electron Paramagnetic Resonance (EPR).

Cytotoxicity of TE agents

MCF 7 and Hela cells were plated and cultured in 96-well microplates (37 °C, 5% CO_2) for 24 hours. Then the $SrTiO_3$ NPs, Cu_2Se QDs or $SrTiO_3/Cu_2Se$ NPs at different concentrations (ranging from 0.025 mg/mL to 0.1 mg/mL) were mixed into the culture medium. Following 24h co-incubation, MTT assay (Life Technologies) was conducted to determine cell viabilities according to the manufacturer's instructions.

Production of ROS in cells

After 24 hours of culture (37 °C, 5% CO_2) in dishes, MCF 7 cells were incubated with the $SrTiO_3$ NPs, Cu_2Se QDs and $SrTiO_3/Cu_2Se$ NPs (final concentration of 0.05 mg/mL) respectively for another 24 hours. Next, the DCFH-DA solution (final concentration of 0.2 μM) was put into the above medium and incubated for 0.5 hours. Following removing the culture medium and washing with PBS, the cells were illuminated for 2.5 min employing an 808 nm light with power 1 W/cm^2 and cooled naturally for 10 min. The green fluorescence induced by ROS was detected by CLSM.

In vitro TET

MCF 7 and Hela cell lines were plated in 96-well plates and cultured for 24 hours (37 °C, 5% CO_2). Then the $SrTiO_3$ NPs, Cu_2Se QDs or $SrTiO_3/Cu_2Se$ NPs at different concentrations (ranging from 0.025 mg/mL to 0.1 mg/mL) were mixed into the culture medium and incubated for another 24 hours. Following culture medium removing and PBS washing, the cells were illuminated for 2.5 min employing an 808 nm light with power 1 W/cm^2 and cooled naturally for 10 min. After 24-hour culture, the cells were washed with PBS for several times. MTT assay was applied to detect cell viability.

Pharmacokinetic study

To conduct in vivo pharmacokinetic study, 200 μL of Cy7 functionalized $SrTiO_3/Cu_2Se$ NPs (5 mg/kg) were i.v. injected in C57BL/6 mice. After different intervals, a microplate reader was utilized to test fluorescent intensity of Cy7 through the collected 20 μL blood.

In vivo imaging and biodistribution study

For the sale of fluorescence imaging and biodistribution study in vivo, 200 μL of Cy7 functionalized $SrTiO_3/Cu_2Se$ NPs (5 mg/kg) were i.v. injected into mice bearing MCF 7 tumors. The Maestro2 In-Vivo Imaging System was employed to detect the fluorescent intensity of tumor and major organs 24 hours post-injection.

In vivo TET

After the tumors had reached to ~100 mm^3, mice were randomly allocated into 6 groups, 5 mice in each group. 1) saline control, 2) $SrTiO_3/Cu_2Se$ NPs, 3) $SrTiO_3$ NPs + DT, 4) Cu_2Se QDs + DT, 5) $SrTiO_3/Cu_2Se$ NPs + DT, 6) G + DT, and 7) PTT (G, >55^oC). The DT means temperature gradient (35-45^oC) for 3 cycles inducing by 808 nm laser irradiation and natural cooling after 24 h post injection The volume of tumors was monitored every two days lasting 14 days.

In vivo toxicity

C57BL/6 mice were i.v. injected with $SrTiO_3/Cu_2Se$ NPs (10 mg/kg) in order for toxicity analysis in vivo. Major organs were collected and subjected to eosin (H&E) and hematoxylin staining 30 days

postinjection. Then the immune response was analyzed through the i.v. injection of $SrTiO_3/Cu_2Se$ NPs (10 mg/kg) into C57BL/6 mice. At 12 hours and 24 hours post-injection, ELISA was used to measure the concentrations of interleukin6 (IL-6), tumor necrosis factor-α (TNF-α) and interferon-γ (IFN-γ). At day1, 7, and 14 after intravenous injection, urea nitrogen (BUN), creatinine (Cr), albumin (ALB), total protein (TP), aspartate alanine aminotransferase (ALT), and aminotransferase (AST) were detected in a whole blood panel.

Statistical analysis

Data statistics and statistical significance were calculated by using Graph Pad Prism 8.0 and Origin 9.0. And NPs biodistribution and tumor volume were analyzed via employing Microsoft Excel 2016.

Declarations

Data availability

The authors declare that all data supporting the findings of this study are available within the article and the Supplementary Information. Other data are available from the corresponding authors upon reasonable request.

Competing interests

The authors declare no competing interests.

Acknowledgments

This study was supported by the National Natural Science Foundation of China (No. 81801826 and 32071322); Science, Technology & Innovation Commission of Shenzhen Municipality (No. JCYJ20180307153300735)

Author contributions

X.J. designed the project. X.J. and C.P. synthesized and characterized the materials. C.P., M. O., and Y. W. performed all the in vitro and in vivo experiments. X.J., Q. X., and L. M. discussed the results and interpreted the data. X.J., Q. X., and L. M. co-wrote the paper, and all authors commented on and approved it.

Statement of ethics approval

All animals received humane care, and the Animal Ethics Committee of Sun Yat-sen University approved all the animal experiments. All experiments were carried out according to the recommendations of the Institutional Animal Care and Use Committee of Sun Yat-sen University (Guangzhou, China).

References

1. Li, J., Cui, D., Jiang, Y., Huang, J., Cheng, P., Pu, K. Near-Infrared Photoactivatable Semiconducting Polymer Nanoblockaders for Metastasis-Inhibited Combination Cancer Therapy. *Adv. Mater.* **31**, 1905091 (2019).
2. Ding, B., Zheng, P., Ma, P. a., Lin, J. Manganese Oxide Nanomaterials: Synthesis, Properties, and Theranostic Applications. *Adv. Mater.* **32**, 1905823 (2020).
3. Li, J., Pu, K. Semiconducting Polymer Nanomaterials as Near-Infrared Photoactivatable Protherapeutics for Cancer. *Accounts Chem Res.* **53**, 752-762 (2020).
4. Wong, X. Y., Sena-Torralba, A., Alvarez-Diduk, R., Muthoosamy, K., Merkoci, A. Nanomaterials for Nanotheranostics: Tuning Their Properties According to Disease Needs. *ACS Nano* **14**, 2585-2627 (2020).
5. Huang, X., Zhang, W., Guan, G., Song, G., Zou, R., Hu, J. Design and Functionalization of the NIR-Responsive Photothermal Semiconductor Nanomaterials for Cancer Theranostics. *Accounts Chem. Res.* **50**, 2529-2538 (2017).
6. Zhao, L., Liu, Y., Xing, R., Yan, X. Supramolecular Photothermal Effects: A Promising Mechanism for Efficient Thermal Conversion. *Angew. Chem. Int. Edit.* **59**, 3793-3801 (2020).
7. Kwon, K. C., Ryu, J. H., Lee, J.-H., Lee, E. J., Kwon, I. C., Kim, K., Lee, J. Proteinticle/Gold Core/Shell Nanoparticles for Targeted Cancer Therapy without Nanotoxicity. *Adv. Mater.* **26**, 6436-6441 (2014).
8. Vijayaraghavan, P., Liu, C.-H., Vankayala, R., Chiang, C.-S., Hwang, K. C. Designing Multi-Branched Gold Nanoechinus for NIR Light Activated Dual Modal Photodynamic and Photothermal Therapy in the Second Biological Window. *Adv. Mater.* **26**, 6689-6695 (2014).
9. Zhang, F., Han, X., Hu, Y., Wang, S., Liu, S., Pan, X., Wang, H., Ma, J., Wang, W., Li, S., Wu, Q., Shen, H., Yu, X., Yuan, Q., Liu, H. Interventional Photothermal Therapy Enhanced Brachytherapy: A New Strategy to Fight Deep Pancreatic Cancer. *Adv. Sci.* **6**, 1801507 (2019).
10. Goncalves, A. S. C., Rodrigues, C. F., Moreira, A. F., Correia, I. J. Strategies to improve the photothermal capacity of gold-based nanomedicines. *Acta Biomater.* **116**, 105-137 (2020).
11. Markovic, Z. M., Harhaji-Trajkovic, L. M., Todorovic-Markovic, B. M., Kepic, D. P., Arsikin, K. M., Jovanovic, S. P., Pantovic, A. C., Dramicanin, M. D., Trajkovic, V. S. In vitro comparison of the photothermal anticancer activity of graphene nanoparticles and carbon nanotubes. *Biomaterials* **32**, 1121-1129 (2011).
12. Zhang, W., Guo, Z., Huang, D., Liu, Z., Guo, X., Zhong, H. Synergistic effect of chemo-photothermal therapy using PEGylated graphene oxide. *Biomaterials* **32**, 8555-8561 (2011).
13. Gan, Z., Wu, X., Meng, M., Zhu, X., Yang, L., Chu, P. K. Photothermal Contribution to Enhanced Photocatalytic Performance of Graphene-Based Nanocomposites. *ACS Nano* **8**, 9304-9310 (2014).
14. Guo, M., Huang, J., Deng, Y., Shen, H., Ma, Y., Zhang, M., Zhu, A., Li, Y., Hui, H., Wang, Y., Yang, X., Zhang, Z., Chen, H. pH-Responsive Cyanine-Grafted Graphene Oxide for Fluorescence Resonance Energy Transfer-Enhanced Photothermal Therapy. *Adv. Funct. Mater.* **25**, 59-67 (2015).
15. Chen, Y.-W., Su, Y.-L., Hu, S.-H., Chen, S.-Y. Functionalized graphene nanocomposites for enhancing photothermal therapy in tumor treatment. *Adv. Drug Deliver. Rev.* **105**, 190-204 (2016).

16. Jia, X., Xu, W., Ye, Z., Wang, Y., Dong, Q., Wang, E., Li, D., Wang, J. Functionalized Graphene@Gold Nanostar/Lipid for Pancreatic Cancer Gene and Photothermal Synergistic Therapy under Photoacoustic/Photothermal Imaging Dual-Modal Guidance. *Small* **16**, 2003707 (2020).
17. Liu, S., Pan, X., Liu, H. Two-Dimensional Nanomaterials for Photothermal Therapy. *Angew. Chem. Int. Edit.* **59**, 5890-5900 (2020).
18. Ji, X., Kong, N., Wang, J., Li, W., Xiao, Y., Gan, S. T., Zhang, Y., Li, Y., Song, X., Xiong, Q., Shi, S., Li, Z., Tao, W., Zhang, H., Mei, L., Shi, J. A Novel Top-Down Synthesis of Ultrathin 2D Boron Nanosheets for Multimodal Imaging-Guided Cancer Therapy. *Adv. Mater.* **30**, 1803031 (2018).
19. Tao, W., Ji, X., Zhu, X., Li, L., Wang, J., Zhang, Y., Saw, P. E., Li, W., Kong, N., Islam, M. A., Gan, T., Zeng, X., Zhang, H., Mahmoudi, M., Tearney, G. J., Farokhzad, O. C. Two-Dimensional Antimonene-Based Photonic Nanomedicine for Cancer Theranostics. *Adv. Mater.* **30**, 1802061 (2018).
20. Ouyang, J., Feng, C., Ji, X., Li, L., Gutti, H. K., Kim, N. Y., Artzi, D., Xie, A., Kong, N., Liu, Y.-N., Tearney, G. J., Sui, X., Tao, W., Farokhzad, O. C. 2D Monoelemental Germanene Quantum Dots: Synthesis as Robust Photothermal Agents for Photonic Cancer Nanomedicine. *Angew. Chem. Int. Edit.* **58**, 13405-13410 (2019).
21. Tao, W., Kong, N., Ji, X., Zhang, Y., Sharma, A., Ouyang, J., Qi, B., Wang, J., Xie, N., Kang, C., Zhang, H., Farokhzad, O. C., Kim, J. S. Emerging two-dimensional monoelemental materials (Xenes) for biomedical applications. *Chem. Soc. Rev.* **48**, 2891-2912 (2019).
22. Feng, C., Ouyang, J., Tang, Z., Kong, N., Liu, Y., Fu, L., Ji, X., Xie, T., Farokhzad, O. C., Tao, W. Germanene-Based Theranostic Materials for Surgical Adjuvant Treatment: Inhibiting Tumor Recurrence and Wound Infection. *Matter* **3**, 127-144 (2020).
23. Ouyang, J., Ji, X., Zhang, X., Feng, C., Tang, Z., Kong, N., Xie, A., Wang, J., Sui, X., Deng, L., Liu, Y., Kim, J. S., Cao, Y., Tao, W. In situ sprayed NIR-responsive, analgesic black phosphorus-based gel for diabetic ulcer treatment. *Proc. Natl. Acad. Sci. U. S. A.* **117**, 28667-28677 (2020).
24. Chen, W., Liu, C., Ji, X., Joseph, J., Tang, Z., Ouyang, J., Xiao, Y., Kong, N., Joshi, N., Farokhzad, O. C., Tao, W., Xie, T. Stanene-Based Nanosheets forbeta-Elemene Delivery and Ultrasound-Mediated Combination Cancer Therapy. *Angew. Chem. Int. Edit.* 10.1002/anie.202016330 (2021).
25. Jiang, Y., Li, J., Zhen, X., Xie, C., Pu, K. Dual-Peak Absorbing Semiconducting Copolymer Nanoparticles for First and Second Near-Infrared Window Photothermal Therapy: A Comparative Study. *Adv. Mater.* **30**, 1705980 (2018).
26. Liu, G., Zhu, J., Guo, H., Sun, A., Chen, P., Xi, L., Huang, W., Song, X., Dong, X. Mo2C-Derived Polyoxometalate for NIR-II Photoacoustic Imaging-Guided Chemodynamic/Photothermal Synergistic Therapy. *Angew. Chem. Int. Edit.* **58**, 18641-18646 (2019).
27. Zhang, H., Zeng, W., Pan, C., Feng, L., Ou, M., Zeng, X., Liang, X., Wu, M., Ji, X., Mei, L. SnTe@MnO2-SP Nanosheet-Based Intelligent Nanoplatform for Second Near-Infrared Light-Mediated Cancer Theranostics. *Adv. Funct. Mater.* **29**, 1903791 (2019).
28. Xu, C., Pu, K. Second near-infrared photothermal materials for combinational nanotheranostics. *Chem. Soc. Rev.* **50**, 1111-1137 (2020).

29. Zhou, H., Zeng, X., Li, A., Zhou, W., Tang, L., Hu, W., Fan, Q., Meng, X., Deng, H., Duan, L., Li, Y., Deng, Z., Hong, X., Xiao, Y. Upconversion NIR-II fluorophores for mitochondria-targeted cancer imaging and photothermal therapy. *Nat. Commun.* **11**, 6183-6183 (2020).
30. Li, J., Jiang, R., Wang, Q., Li, X., Hu, X., Yuan, Y., Lu, X., Wang, W., Huang, W., Fan, Q. Semiconducting polymer nanotheranostics for NIR-II/Photoacoustic imaging-guided photothermal initiated nitric oxide/photothermal therapy. *Biomaterials* **217**, 119304 (2019).
31. Yang, C., Younis, M. R., Zhang, J., Qu, J., Lin, J., Huang, P. Programmable NIR-II Photothermal-Enhanced Starvation-Primed Chemodynamic Therapy using Glucose Oxidase-Functionalized Ancient Pigment Nanosheets. *Small* **16**, 2001518 (2020).
32. Zhang, Q., Guo, Q., Chen, Q., Zhao, X., Pennycook, S. J., Chen, H. Highly Efficient 2D NIR-II Photothermal Agent with Fenton Catalytic Activity for Cancer Synergistic Photothermal-Chemodynamic Therapy. *Adv. Sci.***7**, 1902576 (2020).
33. Zhang, W., Deng, W., Zhang, H., Sun, X., Huang, T., Wang, W., Sun, P., Fan, Q., Huang, W. Bioorthogonal-targeted 1064 nm excitation theranostic nanoplatform for precise NIR-IIa fluorescence imaging guided efficient NIR-II photothermal therapy. *Biomaterials* **243**, 119934 (2020).
34. Zhang, Q., Sun, Y., Xu, W., Zhu, D. Organic Thermoelectric Materials: Emerging Green Energy Materials Converting Heat to Electricity Directly and Efficiently. *Adv. Mater.* **26**, 6829-6851 (2014).
35. Avery, A. D., Zhou, B. H., Lee, J., Lee, E.-S., Miller, E. M., Ihly, R., Wesenberg, D., Mistry, K. S., Guillot, S. L., Zink, B. L., Kim, Y.-H., Blackburn, J. L., Ferguson, A. J. Tailored semiconducting carbon nanotube networks with enhanced thermoelectric properties. *Nat. Energy* **1**, 16033 (2016).
36. Zhang, J., Song, L., Madsen, G. K. H., Fischer, K. F. F., Zhang, W., Shi, X., Iversen, B. B. Iversen, Designing high-performance layered thermoelectric materials through orbital engineering. *Nat. Commun.* **7**, 10892 (2016).
37. Kim, F., Kwon, B., Eom, Y., Lee, J. E., Park, S., Jo, S., Park, S. H., Kim, B.-S., Im, H. J., Lee, M. H., Min, T. S., Kim, K. T., Chae, H. G., King, W. P., Son, J. S. 3D printing of shape-conformable thermoelectric materials using all-inorganic Bi2Te3-based inks. *Nat. Energy* **3**, 301-309 (2018).
38. Ding, Y., Qiu, Y., Cai, K., Yao, Q., Chen, S., Chen, L., He, J. High performance n-type Ag2Se film on nylon membrane for flexible thermoelectric power generator. *Nat. Commun.* **10**, 841 (2019).
39. Qiu, P., Mao, T., Huang, Z., Xia, X., Liao, J., Agne, M. T., Gu, M., Zhang, Q., Ren, D., Bai, S., Shi, X., Snyder, G. J., Chen, L. High-Efficiency and Stable Thermoelectric Module Based on Liquid-Like Materials. *Joule* **3**, 1538-1548 (2019).
40. Wang, Y., Yang, L., Shi, X.-L., Shi, X., Chen, L., Dargusch, M. S., Zou, J., Chen, Z.-G. Flexible Thermoelectric Materials and Generators: Challenges and Innovations. *Adv. Mater.* **31**, 1807916 (2019).
41. Pan, C., Ou, M., Cheng, Q., Zhou, Y., Yu, Y., Li, Z., Zhang, F., Xia, D., Mei, L., Ji, X. Z-Scheme Heterojunction Functionalized Pyrite Nanosheets for Modulating Tumor Microenvironment and Strengthening Photo/Chemodynamic Therapeutic Effects. *Adv. Funct. Mater.* **30**, 1906466 (2019).

42. Zhu, P., Chen, Y., Shi, J. Piezocatalytic Tumor Therapy by Ultrasound-Triggered and BaTiO3 -Mediated Piezoelectricity. *Adv. Mater.* **32**, 2001976 (2020).
43. Chen, R., Lee, J., Lee, W., Li, D. Thermoelectrics of Nanowires. *Chem. Rev.* **119**, 9260-9302 (2019).
44. Tan, G., Zhao, L.-D., Kanatzidis, M. G. Rationally Designing High-Performance Bulk Thermoelectric Materials. *Chem. Rev.* **116**, 12123-12149 (2016).
45. Shi, X.-L., Zou, J., Chen, Z.-G. Advanced Thermoelectric Design: From Materials and Structures to Devices. *Chem. Rev.* **120**, 7399-7515 (2020).
46. Ji, X., Wang, J., Kang, Y., Mei, L., Su, Z., Wang, S., Ma, G., Shi, J., Zhang, S. Enhanced Solar Energy Harvest and Electron Transfer through Intra- and Intermolecular Dual Channels in Chlorosome-Mimicking Supramolecular Self-Assemblies. *ACS Catal.* **8**, 10732-10745 (2018).
47. Ji, X., Kang, Y., Fan, T., Xiong, Q., Zhang, S., Tao, W., Zhang, H. An antimonene/Cp*Rh(phen)Cl/black phosphorus hybrid nanosheet-based Z-scheme artificial photosynthesis for enhanced photo/bio-catalytic CO2 reduction. *J. Mater. Chem. A* **8**, 323-333 (2020).
48. Kang, Y., Li, Z., Yang, Y., Su, Z., Ji, X., Zhang, S. Antimonene Nanosheets-Based Z-Scheme Heterostructure with Enhanced Reactive Oxygen Species Generation and Photothermal Conversion Efficiency for Photonic Therapy of Cancer. *Adv. Health. Mater.* **10**, 2001835 (2020).
49. Ou, M., Pan, C., Yu, Y., Wang, X., Zhou, Y., Zhang, H., Cheng, Q., Wu, M., Ji, X., Mei, L. Two-dimensional highly oxidized ilmenite nanosheets equipped with Z-scheme heterojunction for regulating tumor microenvironment and enhancing reactive oxygen species generation. *Chem. Eng. J.* **390**, 124524 (2020).
50. Pan, C., Ou, M., Cheng, Q., Zhou, Y., Yu, Y., Li, Z., Zhang, F., Xia, D., Mei, L., Ji, X. Z-Scheme Heterojunction Functionalized Pyrite Nanosheets for Modulating Tumor Microenvironment and Strengthening Photo/Chemodynamic Therapeutic Effects. *Adv. Funct. Mater.* **30**, 1906466 (2020).
51. Choi, M. S., Qu, D., Lee, D., Liu, X., Watanabe, K., Taniguchi, T., Yoo, W. J. Lateral MoS2 p-n Junction Formed by Chemical Doping for Use in High-Performance Optoelectronics. *ACS Nano* **8**, 9332-9340 (2014).
52. Deng, Y., Luo, Z., Conrad, N. J., Liu, H., Gong, Y., Najmaei, S., Ajayan, P. M., Lou, J., Xu, X., Ye, P. D. Black Phosphorus-Monolayer MoS2 van der Waals Heterojunction p-n Diode. *ACS Nano* **8**, 8292-8299 (2014).
53. Lee, C.-H., Lee, G.-H., van der Zande, A. M., Chen, W., Li, Y., Han, M., Cui, X., Arefe, G., Nuckolls, C., Heinz, T. F., Guo, J., Hone, J., Kim, P. Atomically thin p-n junctions with van der Waals heterointerfaces. *Nat. Nanotech.* **9**, 676-681 (2014).
54. Frisenda, R., Molina-Mendoza, A. J., Mueller, T., Castellanos-Gomez, A., van der Zant, H. S. J. Atomically thin p-n junctions based on two-dimensional materials. *Chem. Soc. Rev.* **47**, 3339-3358 (2018).
55. Hu, F., Cai, Q., Liao, F., Shao, M., Lee, S.-T. Recent Advancements in Nanogenerators for Energy Harvesting. *Small* **11**, 5611-5628 (2015).

56. Guo, L., Lu, Q. Potentials of piezoelectric and thermoelectric technologies for harvesting energy from pavements. *Renew. Sust. Energ. Rev.* **72**, 761-773 (2017).
57. Bai, Y., Jantunen, H., Juuti, J. Energy Harvesting Research: The Road from Single Source to Multisource. *Adv. Mater.* **30**, 1707271 (2018).
58. Kong, N., Ji, X., Wang, J., Sun, X., Chen, G., Fan, T., Liang, W., Zhang, H., Xie, A., Farokhzad, O. C., Tao, W. ROS-Mediated Selective Killing Effect of Black Phosphorus: Mechanistic Understanding and Its Guidance for Safe Biomedical Applications. *Nano Lett.* **20**, 3943-3955 (2020).

Figures

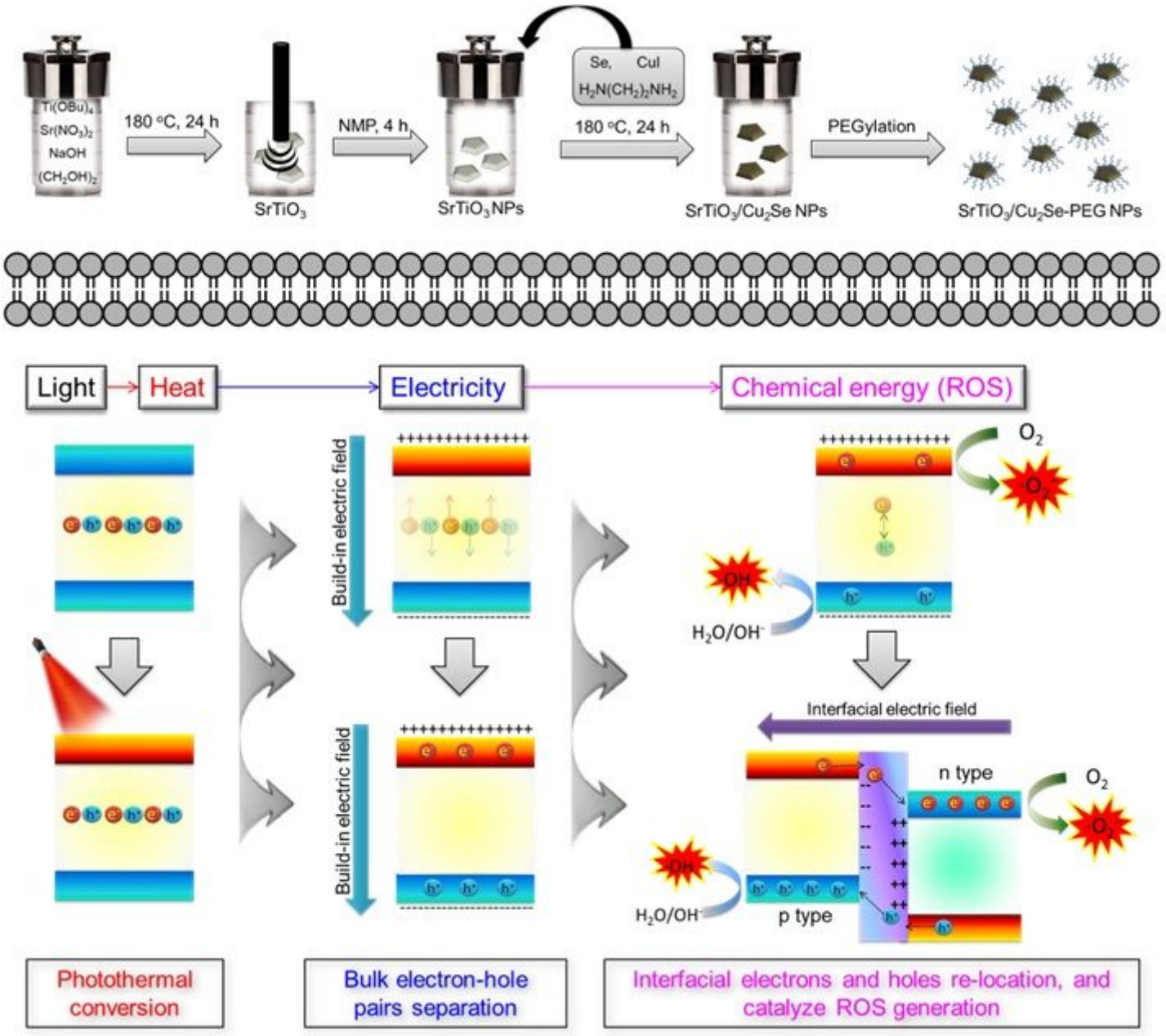

Figure 1

Schematic illustration of preparation and mechanism of SrTiO3/Cu2Se p-n heterojunction based thermoelectric therapy (TET). SrTiO3/Cu2Se p-n heterojunction was fabricated through two steps hydrothermal process.

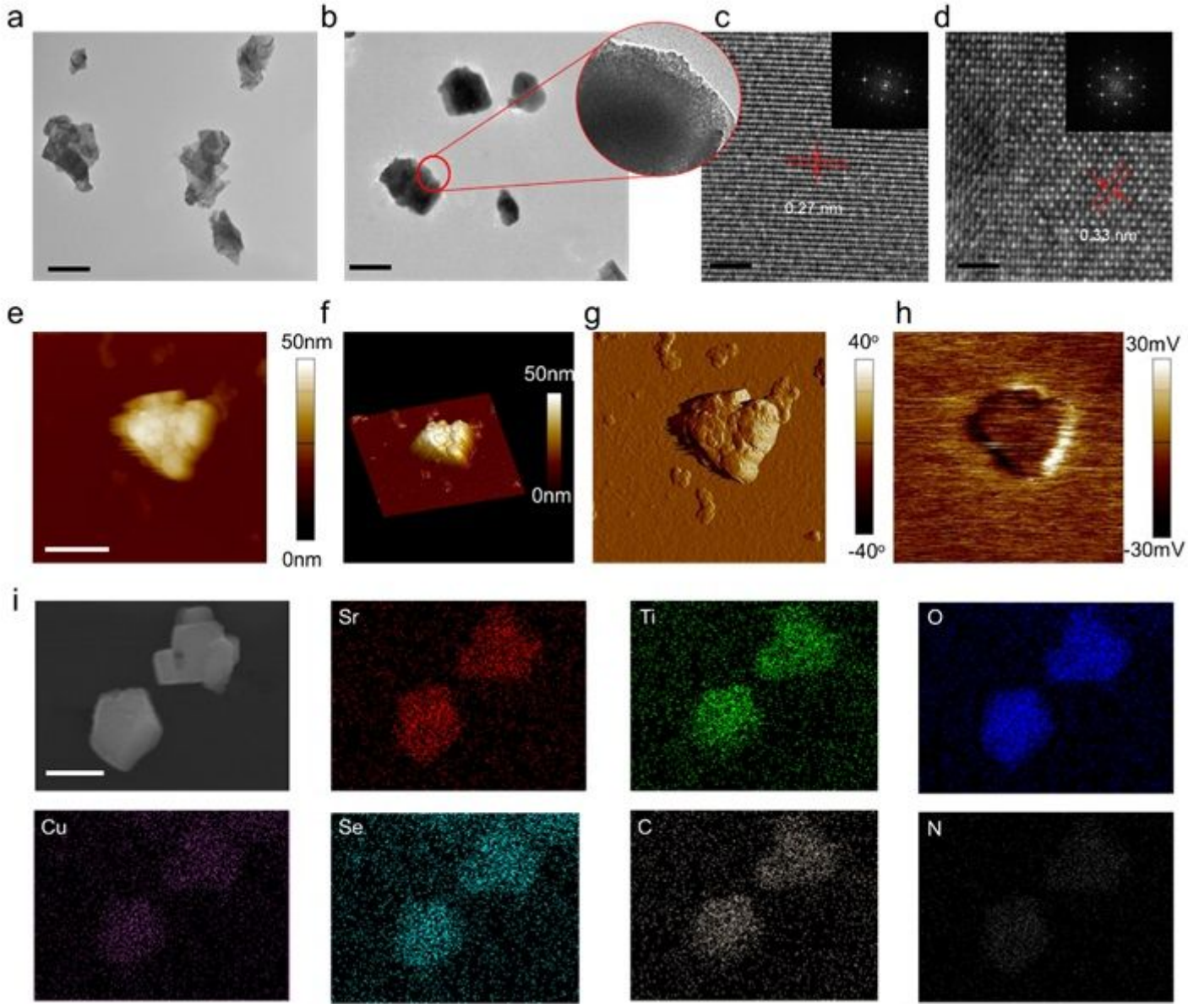

Figure 2

Characterization of SrTiO3/Cu2Se p-n heterojunction. a TEM images of SrTiO3 NSs (scale bar 100 nm). b TEM images of SrTiO3/Cu2Se NSs (scale bar 100 nm). c HRTEM image (inset: FFT diffraction patterns) of SrTiO3 (scale bar 5 nm). d HRTEM image (inset: FFT diffraction patterns) of Cu2Se (scale bar 5 nm). e 2D AFM image of SrTiO3/Cu2Se NSs (scale bar 100 nm for all panels). f 3D AFM image of SrTiO3/Cu2Se NSs. g phase image of the piezoelectric response of SrTiO3/Cu2Se NSs. h piezoelectric potential of SrTiO3/Cu2Se NSs. i SEM-EDX mapping images of SrTiO3/Cu2Se NSs (scale bar 100 nm for all panels).

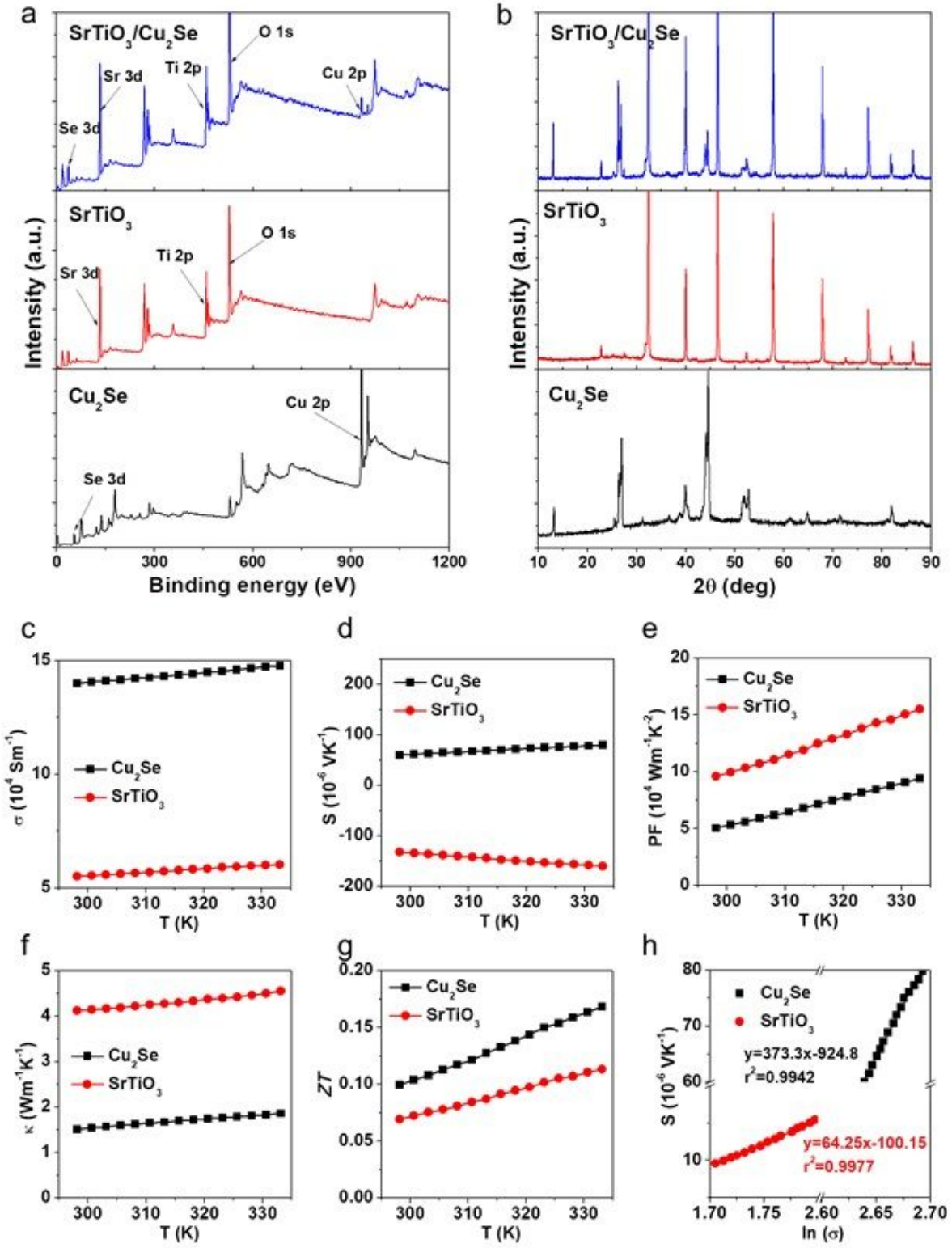

Figure 3

Chemical composition and thermoelectric characterization. a XPS spectra of SrTiO3 NSs, Cu2Se NPs, and SrTiO3/Cu2Se NSs. b XRD spectra of SrTiO3 NSs, Cu2Se NPs, and SrTiO3/Cu2Se NSs. Thermoelectric characteristics of SrTiO3 NSs and Cu2Se NPs: (c) o, (d) S, (e) PF (f) κ, (g) ZT, and (h) S vs ln (o), respectively.

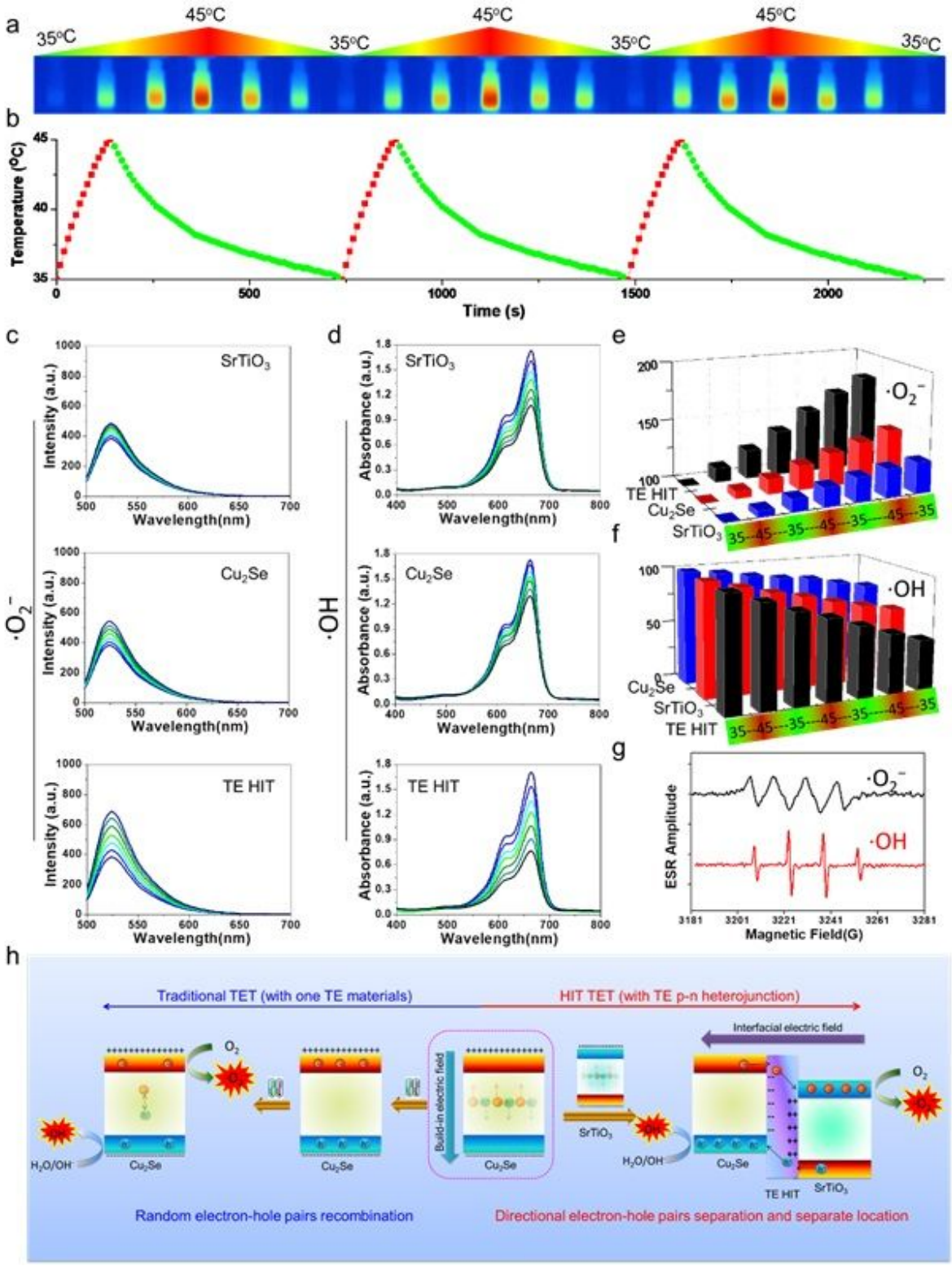

Figure 4

ROS generation and mechanism of TET. a Photothermal images of SrTiO3/Cu2Se NSs under 808 nm laser irradiation. b photothermal conversion of SrTiO3/Cu2Se NSs under 808 nm laser irradiation. c and e ·O2- generation of SrTiO3/Cu2Se NSs under temperature gradient from 35 oC to 45 oC. d and f ·OH generation of SrTiO3/Cu2Se NSs under temperature gradient from 35 oC to 45 oC. g The signal of ROS generated by SrTiO3/Cu2Se NPs in EPR spectra. h The mechanism of SrTiO3/Cu2Se NSs mediated TET.

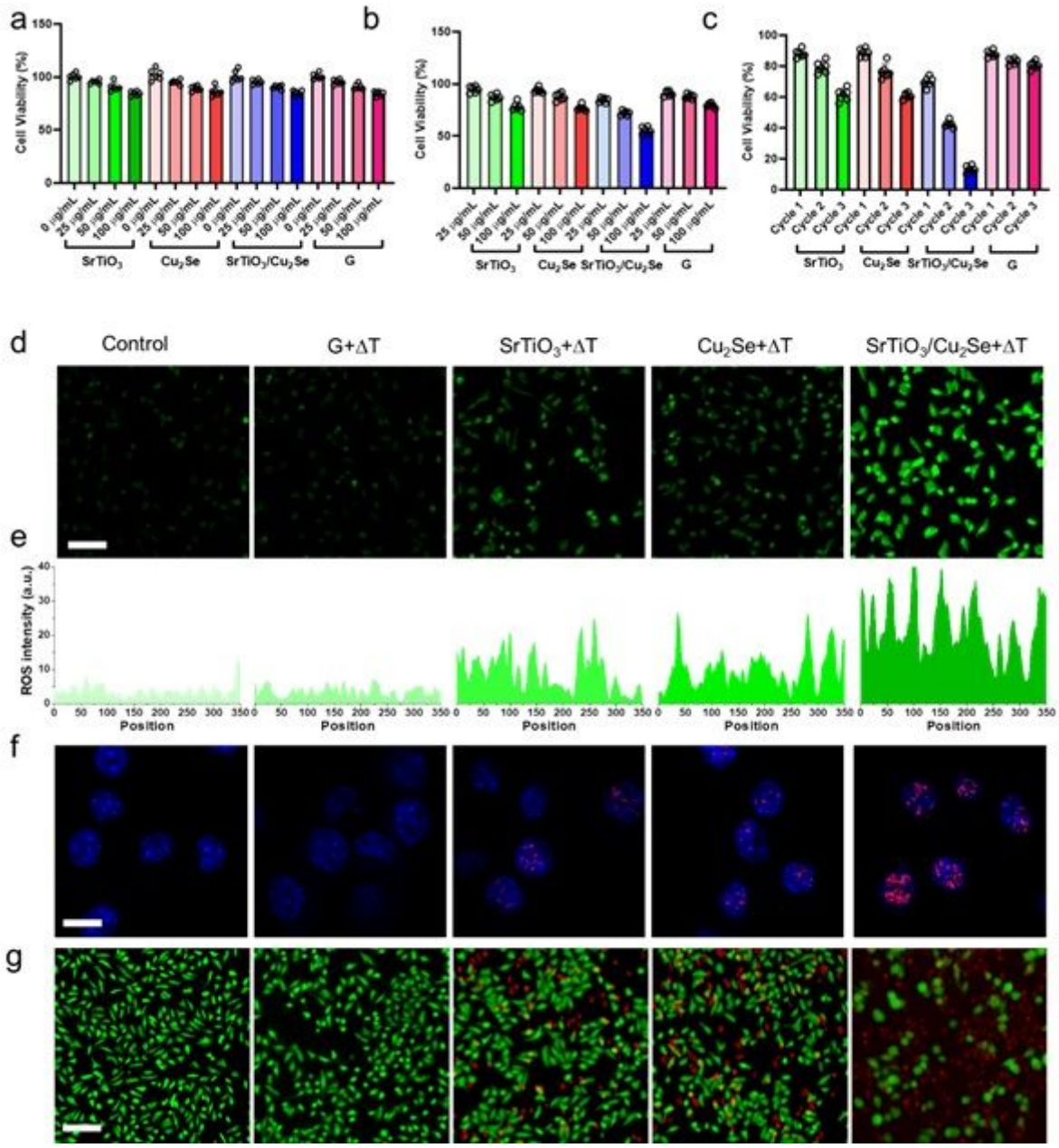

Figure 5

In vitro TET. a Human breast cells (MCF 7) viability treated with SrTiO3 NSs, Cu2Se NPs, and SrTiO3/Cu2Se NSs at different concentrations for 24 h. The data show mean ± s.d., n = 6 biologically independent cells. b human breast cancer cells (MCF 7) viability treated with SrTiO3 NSs, Cu2Se NPs, and SrTiO3/Cu2Se NSs and 808 nm laser at different concentrations for 24 h. The data show mean ± s.d., n = 6 biologically independent cells. c Antitumor effect of SrTiO3 NSs, Cu2Se NPs, and SrTiO3/Cu2Se NSs based TET under different temperature gradient cycles. The data show mean ± s.d., n = 6 biologically independent cells. d CLSM images of ROS content in MCF 7 cells under different treatments. Scale bar = 100 μm. e Fluorescence quantitative analysis of the intracellular ROS in Figure d. f Representative CLSM images of the MCF 7 cells after different treatments. Scale bar = 20 μm. The nuclei were stained by DAPI (blue), and the γH2AX foci per nucleus were stained by anti-γH2AX antibody (red). g Live/Dead cell

staining assay in MCF 7 cells after different treatments (green, live cells; red, dead cells). Scale bar = 100 μm.

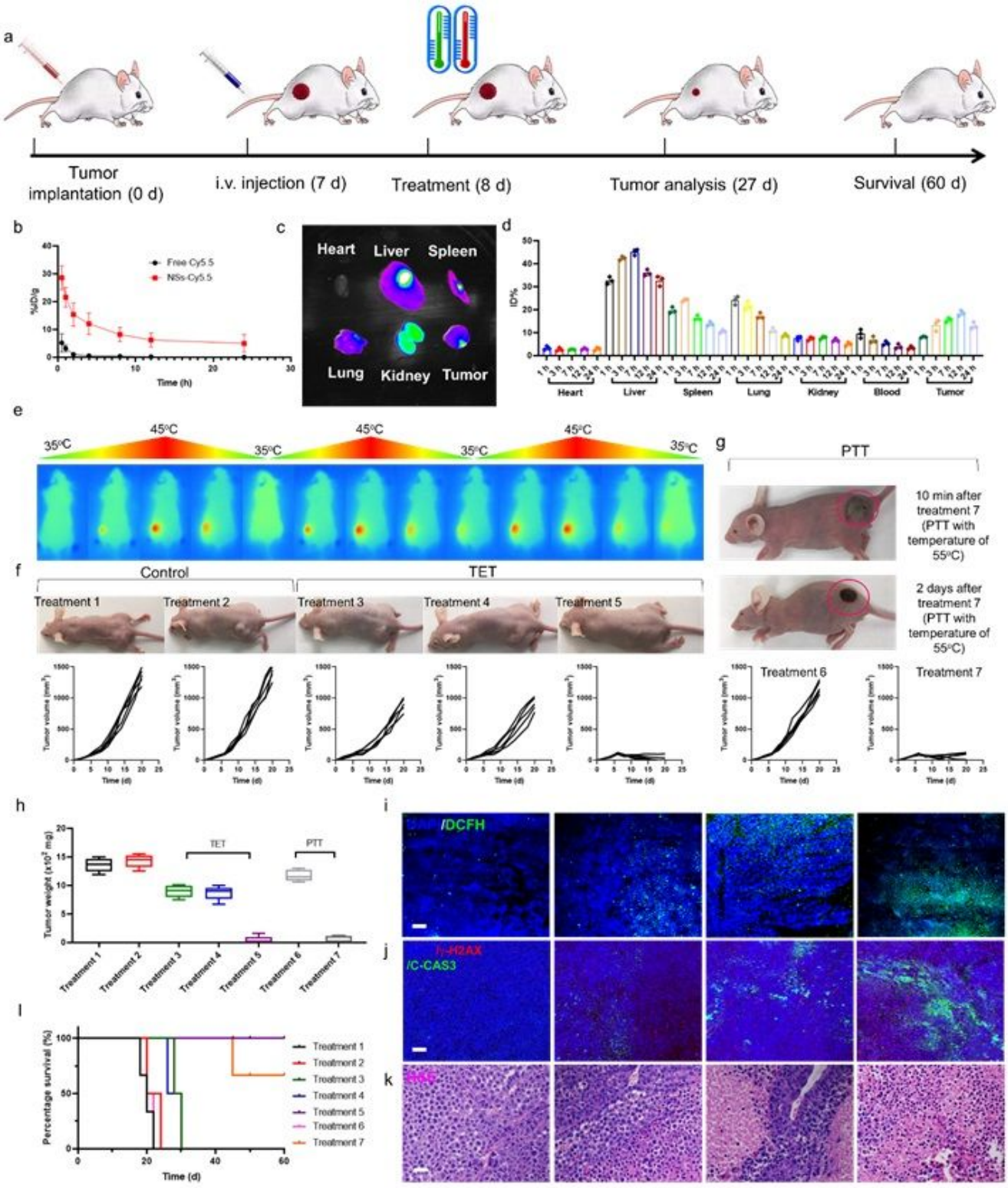

Figure 6

In vivo imaging, biodistribution, and anti-tumor study. a Schematic illustration of treatment schedule. b Blood circulation performance of NPs-Cy7 and free Cy7. The data show mean ± s.d., n = 3 biologically independent animals. c Fluorescence images of major organs with i.v. injection of Cy 7 functionalized

SrTiO3/Cu2Se NPs. d Biodistribution of SrTiO3/Cu2Se NPs in MCF 7 tumor-bearing mice by ICP measurement. The data show mean ± s.d., n = 3 biologically independent mice. e Photothermal heating and natural cooling images of tumor-bearing nude mice. f Anti-tumor effects of TET. Treatment 1: PBS, Treatment 2: SrTiO3/Cu2Se NPs, Treatment 3: SrTiO3 NSs + DT, Treatment 4: Cu2Se NPs + DT, and Treatment 5: SrTiO3/Cu2Se NPs + DT. g Traditional graphene mediated PTT. Treatment 6: graphene with temperature increase to 45 oC and Treatment 7: graphene with temperature increase to 55 oC. h Tumors weight after different treatments. The data show mean ± s.d., n = 5 biologically independent mice. i In vivo ROS detection in the sections from tumors by dihydroethidium (DHE) via fluorescence microscopy. j Immunofluorescence (IF) k H&E staining in the sections from the tumors after different treatments. The nucleus was stained by DAPI (blue), damaged DNA was stained by γH2AX foci (red), and apoptotic cells were stained by apoptosis marker C-CAS3 (green). Scar bar = 100 μm. Three times each experiment was repeated independently with similar results. l The survival curves of MCF 7 tumor-bearing mice after different treatments.

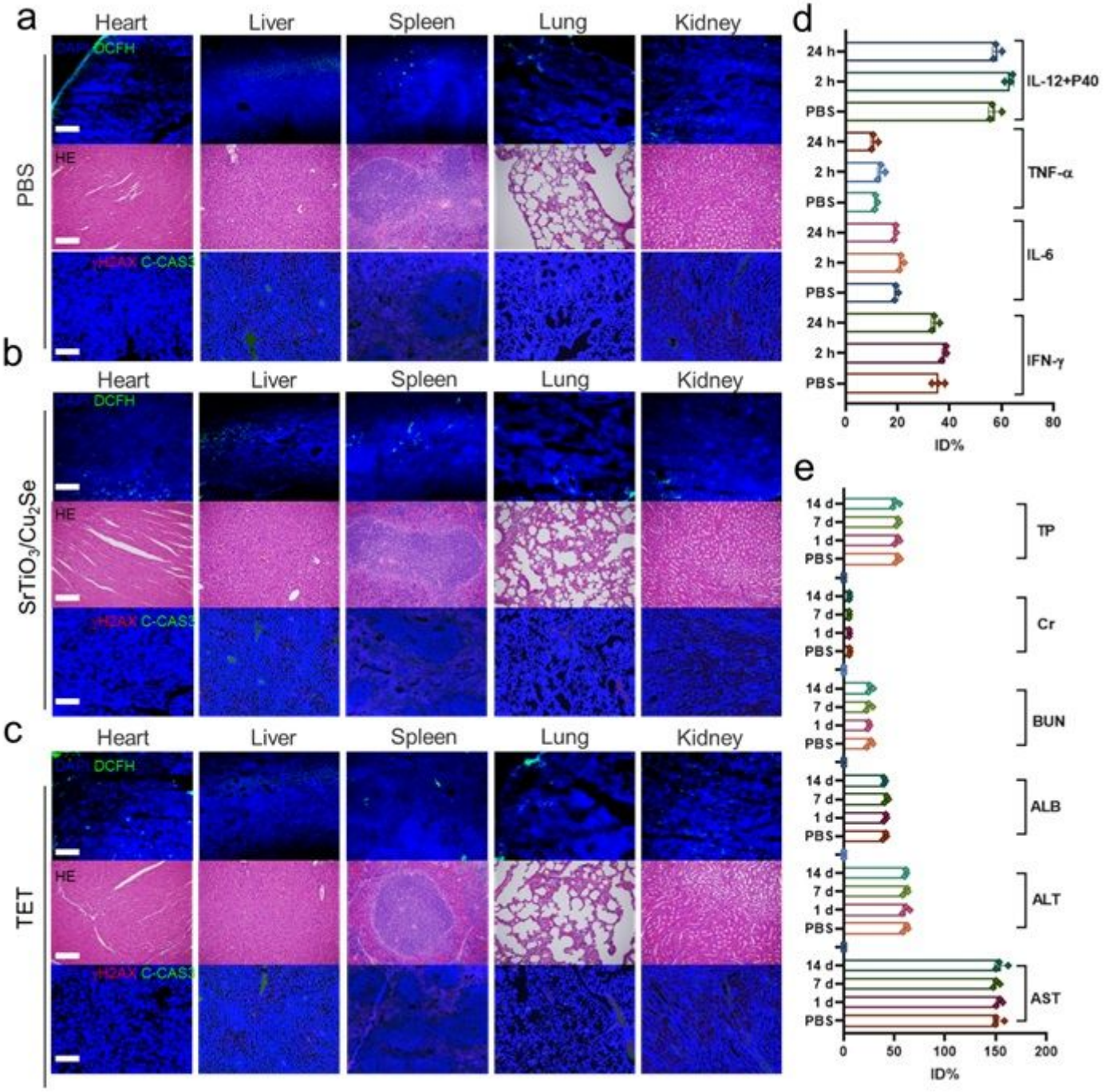

Figure 7

In vivo toxicity of SrTiO3/Cu2Se NPs and SrTiO3/Cu2Se NPs mediated TET. H&E staining and immunofluorescence (IF) staining in the sections from the major organs, which were collected from the MCF 7 xenograft-tumor bearing mice after different treatments with a PBS, b SrTiO3/Cu2Se NPs, and c SrTiO3/Cu2Se NPs mediated TET. The nucleus was stained by DAPI (blue), damaged DNA was stained by γH2AX foci (red), and apoptotic cells were stained by apoptosis marker C-CAS3 (green). Scar bar=100 μm. Three times each experiment was repeated independently with similar results. d Serum levels IFN-γ, IL-6, TNF-α, and IL-12+P40 in healthy mice at 2 or 24 h post intravenous injection of PBS or

SrTiO3/Cu2Se NPs. e Blood biochemistry and hematology analysis of Balb/c mice treated with PBS or SrTiO3/Cu2Se NPs.

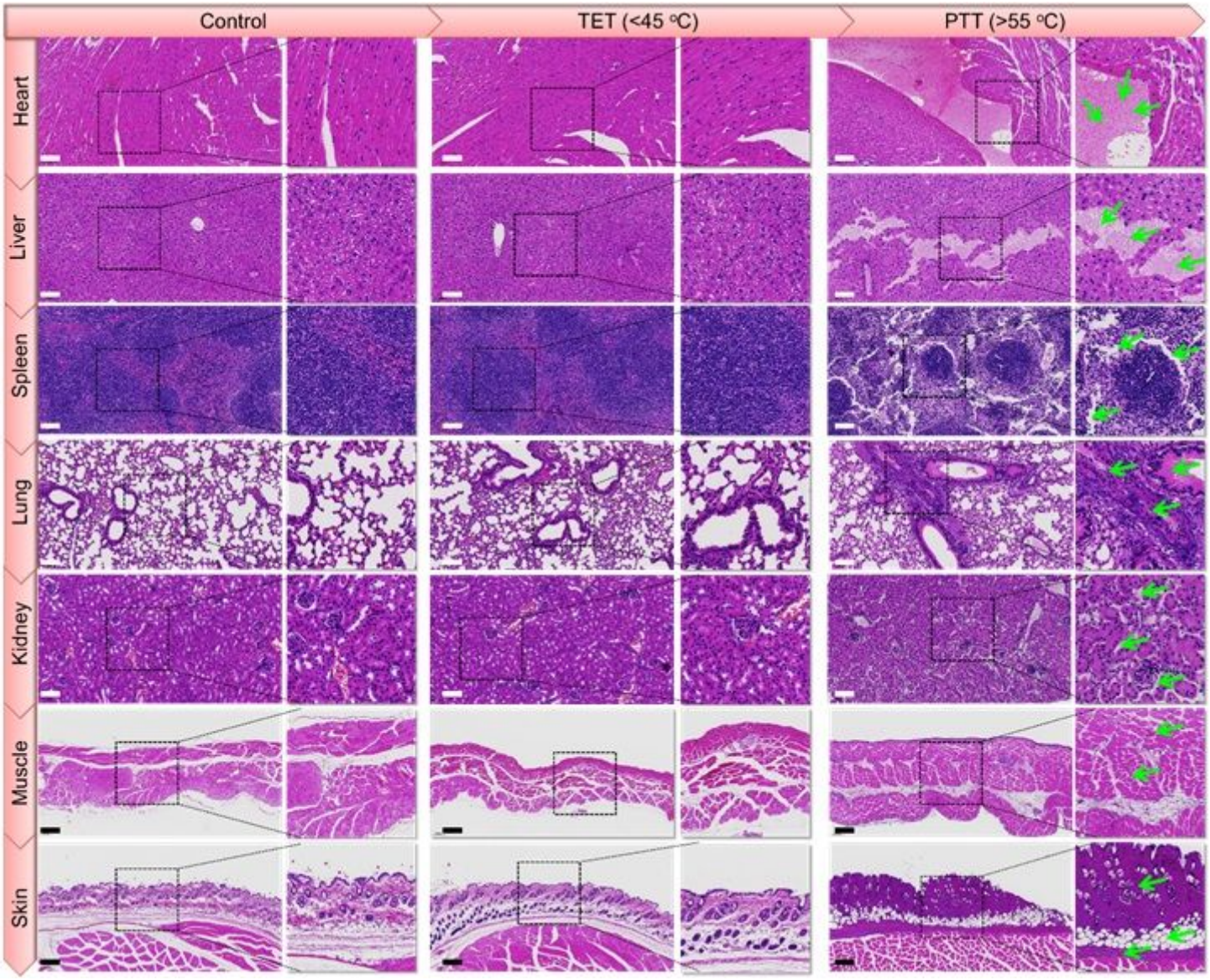

Figure 8

H&E staining of major organs and tissues contacted with different temperature stimulating the potential damages of TET and traditional PTT to nearby organs and tissues. Scar bars = 500 μm.

Supplementary Files

This is a list of supplementary files associated with this preprint. Click to download.

- SI.docx